Journal of Biomedical Optics 10(2), 024020 (March/April 2005)

Phase shifting speckle interferometry for determination of strain and Young's modulus of mineralized biological materials: a study of tooth dentin compression in water

Paul Zaslansky
Weizmann Institute of Science
Department of Structural Biology
Rehovot, Israel 76100
E-mail: paul.zaslansky@weizmann.ac.il

John D. Currey
University of York
Department of Biology
York YO10 5YW, United Kingdom

Asher A. Friesem
Weizmann Institute of Science
Department of Physics of Complex Systems
Rehovot, Israel 76100

Steve Weiner
Weizmann Institute of Science
Department of Structural Biology
Rehovot, Israel 76100
Tel. +972-8-9342552, Fax: 972-8-9344136

Abstract. Mineralized biological materials have complex hierarchical graded structures. It is therefore difficult to understand the relations between their structure and mechanical properties. We report the use of electronic speckle pattern-correlation interferometry (ESPI) combined with a mechanical compression apparatus to measure the strain and Young's modulus of root dentin compressed under water. We describe the optomechanical instrumentation, experimental techniques and procedures needed to measure cubes as small as 1×1×2 mm. Calibration of the method is performed using aluminum, which shows that the measurements are accurate within 3% of the compression modulus reported for standard aluminum 6061. Our results reveal that the compression moduli of root dentin from the buccal and lingual sides of the root are quite different from the moduli of the interproximal sides. Root dentin from interproximal locations is found to have an average modulus of 21.3 GPa, which is about 40% stiffer than root dentin from the buccal and lingual locations, found to have a modulus of 15.0 GPa. Our approach can be used to map deformations on irregular surfaces, and measure strain on wet samples of varying sizes. This can be extended to the study of other biological materials including bone and synthetic biomaterials. *© 2005 Society of Photo-Optical Instrumentation Engineers.* [DOI: 10.1117/1.1891505]

Keywords: electronic speckle pattern-correlation interferometry; dentin; compression elastic modulus.

Paper 04107 received Jun. 23, 2004; revised manuscript received Sep. 5, 2004; accepted for publication Sep. 16, 2004; published online Apr. 26, 2005.

1 Introduction

Mineralized biological materials have complex structures ranging in scale from nanometers to centimeters. Many of these materials have both hierarchical and graded structures, which form the basis for their unique mechanical properties.[1] Bone and tooth dentin are representatives of such mineralized biological materials[2,3] that perform key mechanical functions in the vertebrates. They are composed of protein fibers of type 1 collagen, water, and the mineral carbonate-hydroxylapatite, the proportions of which can vary in different locations.[4] Their mechanical properties, particularly at the intermediate mesoscale, are still poorly understood. Here we use digital interferometry to study elastic compression at the mesoscale of tooth root dentin.

Many mechanical test methods, such as bending or tension, have been used for measuring samples of bone and dentin, usually with dimensions of several millimeters or more.[5–7] Results of such tests show that these materials have marked mechanical anisotropy, and that a strong link exists between elastic, postyield, and fracture properties and the mineral content.[8] On the submicron scale, nanoindentation techniques have been used to measure the elastic modulus over small areas of a few hundred square nanometers.[9–12] Results of mechanical measurements made in the intermediate mesoscale, namely in the submillimeter to micron scale, are often conflicting.[6,13] This is the scale at which these materials exhibit significant structural differences that affect their function. It is particularly important to understand the structure-mechanical relations at this meso-scale level.

To characterize the structure and explore the mechanical properties of bone and dentin, various approaches have been reported.[3,13–16] These include Fourier-transform infrared spectroscopy, small-angle x-ray scattering, backscattered electron imaging, and nanoindentation to measure the microstructure and mechanical properties;[3] digital photoelasticity, fluoroscopic x-ray microscopy, and microindentation to measure the mineral and mechanical gradients;[13] scanning acoustic microscopy and Raman spectroscopy for mapping the elastic

---

Address all correspondence to Paul Zaslansky, Structural Biology, Weizmann Institute of Science, Rehovot, 76100 Israel; Tel: +972-8-934-2617; Fax: +972-8-934-4136; E-mail: paul.zaslansky@weizmann.ac.il

1083-3668/2005/$22.00 © 2005 SPIE

constants of dentin immersed in water;[14,15] and Moiré interferometry for measuring dehydration[16] and mechanical[17] strains in teeth. These approaches did not achieve direct, noncontact measurements of deformation in response to mechanical compression. Optical full-field metrology techniques are suited for direct measurements of deformation, and they can be adapted to measure a variety of samples of different sizes. Such optical techniques include speckle shearing interferometry for measuring surface flaws and strains, electronic/digital speckle pattern-correlation interferometry (ESPI/DSPI), and digital holographic phase shifting interferometry for measuring surface displacements.[18,19]

Compared to other methods, optical techniques that measure surface displacements possess many advantages. They are noncontact, they provide the flexibility to choose a variety of gauging reference lengths, and they enable the multiple simultaneous measurement of nanometer-sized displacements over large areas. To date, a number of these methods have been exploited to measure deformations of large samples of bone[20,21] and tooth dentin,[22] but these studies did not include quantitative analysis of strain distributions and Young's modulus on hydrated samples. This may be due to the observed frequent fluctuations of speckle intensities reported for images of wet biological samples.[23] Interestingly, these fluctuations have been analyzed for 1-D speckle patterns and were used for strain measurements on cortical bone and vascular tissue.[24–26]

In this study, phase-shifting speckle interferometry techniques were adapted for measuring the strain and elastic modulus of small, millimeter-sized, wet dentin samples loaded in compression. Despite considerable technical challenges, the measurements were performed on samples that were fully immersed in water. Water is an essential requirement for biological samples that function in an aqueous environment, because water is one of the major components of these materials, and their mechanical properties change considerably if they become dry.[2,5] We describe the integrated optomechanical instrumentational setup, the experimental techniques and calibration procedures, and present the first results of strain and compression elastic modulus determined for human tooth dentin using this approach.

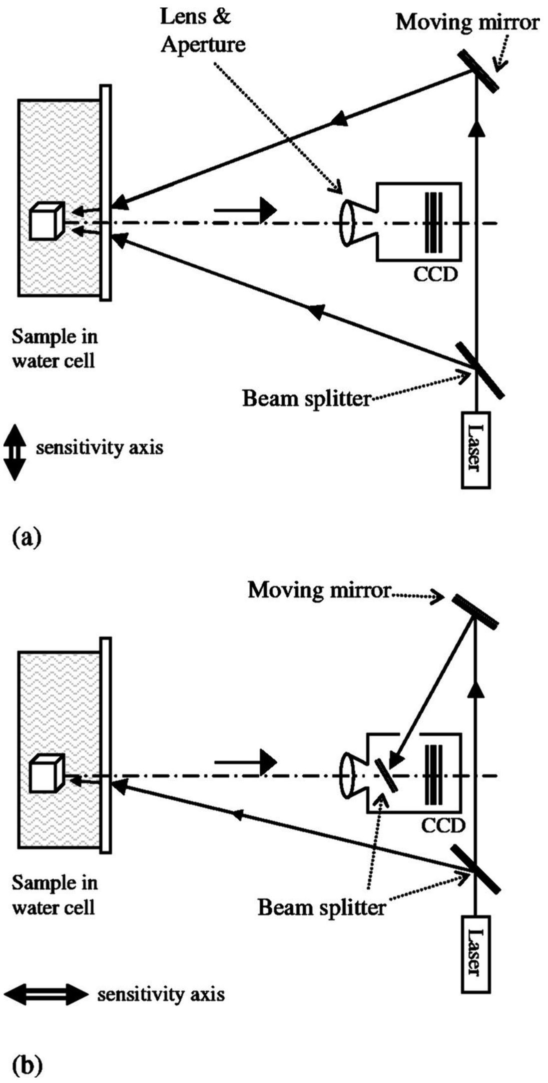

Fig. 1 Interferometric configurations for measuring in-plane and out-of-plane displacements: (a) configuration for the in-plane (X or Y axis) lateral measurements, parallel to the CCD array plane, and (b) configuration for the out-of-plane axial (Z axis) measurements orthogonal to the CCD array plane.

2 Speckle Interferometers for Displacement and Strain Measurements

For more than two decades, a variety of methods have been proposed for measuring surface displacements by means of laser speckles.[18,19] Of these we chose the ESPI method, occasionally denoted digital holography[27] or electro-optic holography,[28] in which the output imagery from computer-controlled laser speckle interferometers is used to map surface displacements.[29]

Displacements on rough surfaces of 3-D samples can be measured independently along three orthogonal axes, X, Y, and Z, by rapidly switching between three separate interferometers. Two different interferometer configurations, shown in Fig. 1, are used. One is used for measuring the out-of-plane displacements along the Z axis [Fig. 1(b)]. Here the light is split into two beams, one of which illuminates the sample while the other is directed toward a CCD detector array and serves as a reference beam. The light reflected from the sample forms a speckle field that interferes at the CCD plane with the reference beam. The other interferometer configuration is used for measuring the in-plane displacements along the X or Y axes [Fig. 1(a)]. Here the light is also split into two beams, both of which illuminate the sample from two opposite symmetric angular orientations, and the reflected light is detected on the CCD plane where the two speckle light fields interfere. Identical interferometer configurations are used for measuring the X and Y axes displacements. In all the interferometers, the optical path of one of the beams is varied by moving a mirror that is mounted on a piezoelectric element and is used to shift the phase of the light field.

The intensity of light detected across the CCD array plane varies spatially in a stochastic manner. This is caused by fluctuations of the light amplitude and phase when laser light is reflected from the surface of the sample. On each detector of the CCD array, the combined light intensity I_{total} at any wavelength λ is

$$I_{\text{total}}=I_a+I_b+2\sqrt{I_aI_b}\cos(\varphi_a-\varphi_b), \tag{1}$$

where I_a and I_b represent the intensities at each point of the interfering beams a and b, and φ_a and φ_b represent the corresponding arbitrary phases at that same point. Although these phases are arbitrary, the difference between them, $\Delta\varphi_{ab}=\varphi_a-\varphi_b$, is constant for a specific imaged point on a static sample. It is possible to determine $\Delta\varphi_{ab}$ by acquiring images using the four-frame algorithm,[30] where the phase of one beam is varied (using the piezoelectric elements) by $\pi/2$, π, $3\pi/2$, and 2π. As a result of this phase stepping, on every detector we obtain four values for I_{total}, denoted by I_1, I_2, I_3, and I_4. $\Delta\varphi_{ab}$ is found from

$$\Delta\varphi_{ab}=\arctan\left[\frac{I_1-I_3}{I_2-I_4}\right]. \tag{2}$$

It is possible to determine the displacements at each point on the sample surface as a result of loading, by determining $\Delta\varphi_{ab}$ pre- and also postloading. Any difference between the two $\Delta\varphi_{ab}$ values, i.e., $\Delta\varphi_{\text{post}}-\Delta\varphi_{\text{pre}}$, will be linearly related to the object sample surface displacement, modulo 2π. By subtracting these phase differences, a map of fringes forms wherever a wrapping of the phase occurs. To recover the true phase, automatic fringe counting (N) and unwrapping is performed.[31] At each point the displacements for the X and Y in-plane interferometers (u and v, respectively) are then obtained from

$$u,v=\frac{N\lambda\cdot(\Delta\varphi_{\text{post}}-\Delta\varphi_{\text{pre}})}{4\pi\cdot\sin\theta}, \tag{3}$$

θ being the angle of illumination relative to the Z axis. The displacements for the Z out-of-plane interferometer (w) are obtained from

$$w=\frac{N\lambda\cdot(\Delta\varphi_{\text{post}}-\Delta\varphi_{\text{pre}})}{4\pi}. \tag{4}$$

The resulting displacement map can now be exploited to derive the strain of the sample by calculating the gradient in the displacements as is observed relative to a common zero point. This is done on the assumption that adjacent points that are mechanically coupled in an elastic material displace in a continuous manner. Axial and shear strain can be calculated from the gradients in the displacements along the X and Y coordinates.[32] Finally, to determine the stress-strain relations of the sample, measurements and gradient calculations are performed for a series of load increments. Young's modulus can then be determined from the slope of stress versus cumulative strain curves.

3 Experimental Setup

Our experimental setup was built in the arrangement shown in Fig. 1. It consists of an optical head and a mechanical compression apparatus. The whole setup is enclosed in an acoustically insulated box that is mounted on a vibration damping sand bed on top of a floating optical table.

The optical head is comprised of three interferometers, all of which are aligned with the laser source and the CCD array that detects the interference speckle images (Q300, Ettemeyer AG, Ulm, Germany). The light source is a 50-mW laser diode with $\lambda=780$ nm, and the CCD detector array has 768×576 detectors, but typically only a subset is used to capture images of the sample. A computer sequentially activates the three interferometers by controlling the laser shutters, the piezo-movable mirrors for phase shifting, and the CCD detector array for image acquisition.

The mechanical compression apparatus, shown in Fig. 2, includes a water cell that can be easily disassembled to facilitate sample mounting, aligning, and cleaning. It was constructed from a modified commercial materials tester (Minimat, Piscataway, New Jersey, Rheometrics) and a custom-built vertical displacement rack with precision positioning rails that prevent any horizontal displacements of the water cell while it is being displaced upward or downward. One side of the water cell is a high-quality glass window (BK-7 λ/10 grade) $100\times78\times2$ mm mounted orthogonal to the optical axis of the CCD detector array. All parts of the water cell that bear significant load are made from stainless steel SS 316 or SS 304.

To minimize torsion, spurious displacements, and bending, a ball bearing is used to transfer force from a load bar to the water cell base and lower anvil pushing them toward the upper anvil. By measuring the displacements of the water cell base as well as the force, it is possible to monitor the extent and rate at which stress develops. The force is applied with the aid of a stepper motor, and it is possible to obtain submicron axial displacements of approximately 750 nm each. Due to mechanical inaccuracies of the motor and gear system, the precise displacement magnitude cannot be set in advance, but can be precisely established after completion of a displacement step. To determine the precise vertical position, we use a high-precision linear variable differential transformer (DCTH1000C LVDT, RDP Electronics, United Kingdom), which is calibrated by a digital encoder (LS803 encoder, VRZ730 display unit, Heidenhain, Germany). With these we are able to measure submicrometer displacements to a resolution of 100 nm. The sand bed serves to dampen any vibrations caused by the motor and drive shafts during each compression increment. The loading components are further stabilized by fixing them to the optical head.

The need for immersing biological samples in water at room temperature (20 to 25°C) causes special difficulties. As shown in Fig. 1, light from the laser sources propagates through air, and then after passing through the glass window it propagates through 48 mm of water prior to impinging on the sample. The light is then reflected from various depths (depending on the sample surface topography and translucency) and propagates back through the water, glass, and air before finally reaching the lens and the CCD array. It is customary and reasonable to neglect the effect of air on light scatter and random variations in phase. However, the water and two additional reflecting interfaces (air-glass and glass-water, respectively) introduce additional random variations to the phase and reduce the amplitude of the light. The water depth of 48 mm is an empirical design compromise, which allows mechanical loading of the water-immersed samples while ensuring that the light reflected from the glass surface is defocused.

The reduction in the amplitude of light mentioned before is constant for a given series of measurements. It results in the

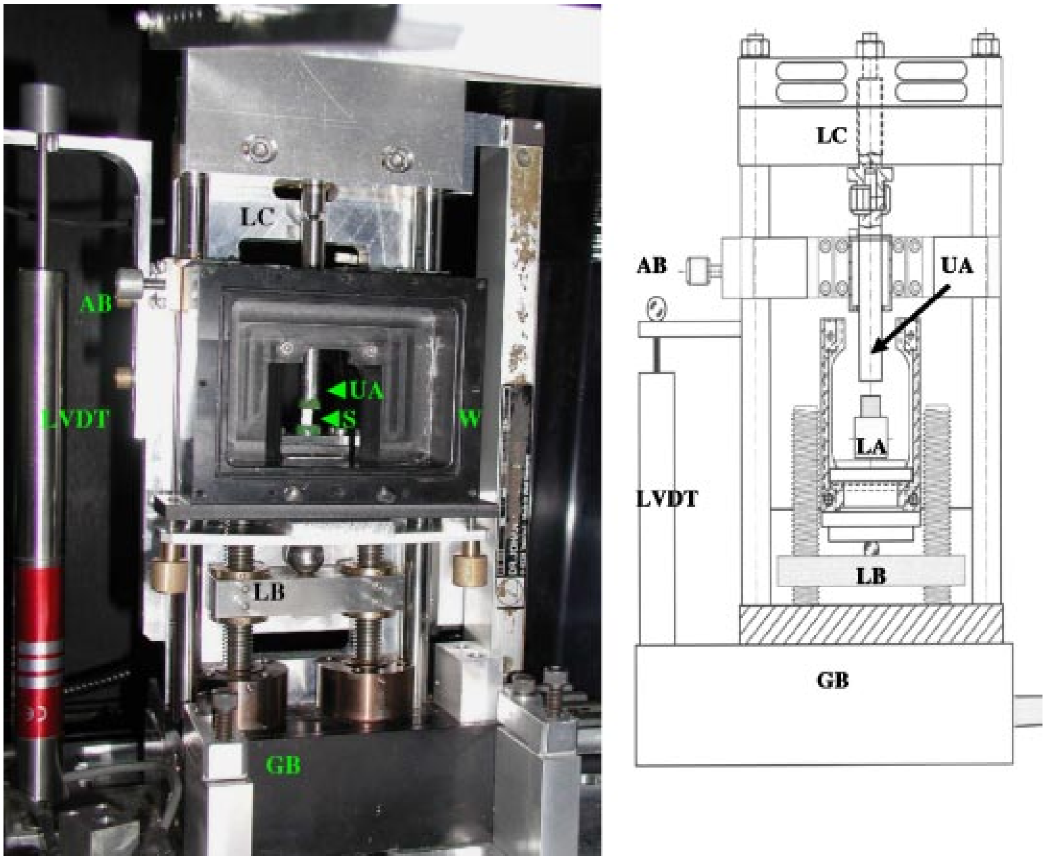

Fig. 2 Mechanical compression apparatus. LC is the load cell and load spring, AB is the alignment bar and upper anvil holder, UA is the upper anvil, LA is the lower anvil, LB is the load-bearing compression bar, GB is the gear box, and LVDT is a linear variable differential transformer for precise axial displacement determination. An object sample (*S*) placed in the water cell (*W*) is compressed to determine surface strain.

degradation of the signal-to-noise ratio as compared with measurements performed without water, because the contrast of the speckles is reduced. The contrast can be improved somewhat by enlarging the imaging lens aperture (as we use the maximum laser power available in the system), but this results in a reduction of the sizes of the speckles and also restricts the depth of field due to a reduced range of focus. Consequently, homogenous illumination becomes difficult to achieve.

The time-dependent random variations in the phase of speckles from the immersed objects merit additional consideration.[23] We believe that this phenomenon can be attributed to turbulence and convection currents in subvolumes of the water. Such variations induce substantial fluctuations in intensity over time, which result in decorrelation between the four sequential intensity measurements used to derive the desired phase differences. The difference $\Delta\varphi_{\mathrm{pre}}-\Delta\varphi_{\mathrm{post}}$ measured before and after compression loading will thus be further modulated by phase variations caused by the water. This may significantly obscure phase shifts attributable to variations in surface topography and makes the detection of displacements technically difficult. Nevertheless, we found that despite the rather slow rate of image acquisition (12 frames/sec), small differences in the optical path length brought about by surface deformation can be reliably detected despite some speckle decorrelation. Specifically, we restricted the object sample deformation to about 2 μm per deformation increment. We found that our conventional CCD array speed was sufficient to measure strains of hard tissues, and expect that with improved CCD arrays of faster acquisition rates, the signal-to-noise ratio can be improved.

If the distance between the sample and the imaging lens is much larger than the sample dimensions, then paraxial approximations hold and no corrections are required for geometry. Indeed, there is no need for matching the refractive index of the glass, water, and air, because they lie along the camera axis in our system.

4 Experimental Procedures

Measurements of strain were first performed on small samples of compressed aluminum to establish the accuracy of the system and optimize the experimental conditions and analysis procedures. These were then applied to measurements of tooth dentin. Aluminum is homogenous, isotropic, and has a known value of Young's modulus. This data was used to calculate the expected gradient of displacements on the surfaces of stressed samples and could be compared with the experimental results. Using the aluminum calibrated system, experimental measurements of dentin samples were carried out. All the experiments more or less simulate normal functioning physiological conditions that exist for root dentin in the oral cavity, namely repeated vertical compression increments, using small loads while keeping the sample wet.

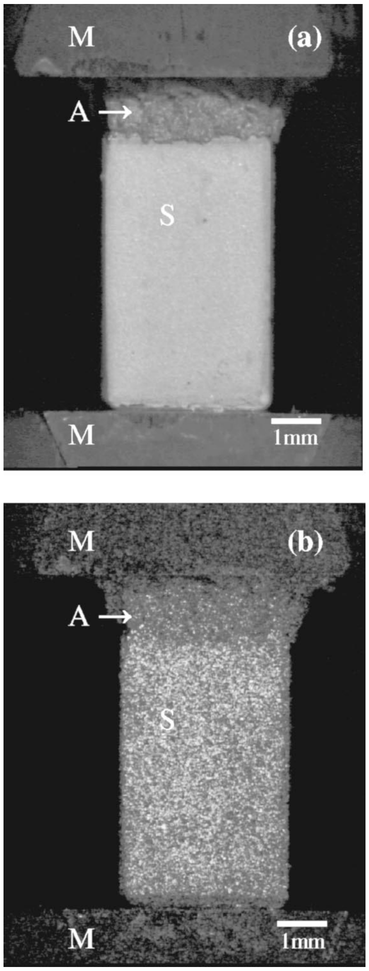

Fig. 3 Aluminum cube under compression: (a) mounted aluminum cube prior to laser illumination, and (b) image of the interference of two superimposed speckle fields on the mounted aluminum cube. A is the amalgam cap, M are the stainless-steel mounting anvils, and S is the aluminum cube sample.

4.1 *Calibration with Aluminum Samples*

Small aluminum cubes (aluminum 6061 T651) with dimensions of 5×4×3 mm were used for calibration. Their dimensions were somewhat larger than those of the dentin samples, but they served well for the purpose of adjusting the mechanics and optics. The samples were loaded along the long axis, so that the cross-sectional area (A) over which loading occurred was $A=4\times3=12\,\text{mm}^2$. The surfaces of the cubes were sprayed with a thin layer of white paint to obtain diffuse reflections of the laser light.

To ensure that the compression load is uniformly applied to the upper and lower surfaces of the aluminum cubes along a vertical axis, we deposited a layer of freshly mixed metallic dental amalgam (GS-80 SDI LTD, Victoria, Australia) triturated for 20 sec on top of the cubes prior to mounting in the mechanical compression apparatus. The aluminum cube was placed on the lower anvil, and its upper surface with the soft amalgam was immediately brought into contact with the upper anvil, as shown in Fig. 3. The amalgam was then allowed to set and harden for at least 24 h. In this way a secure contact between the anvils and the aluminum cube was formed, which enabled an axial transfer of the load. Such cumbersome mounting was necessary to overcome the subtle deviations from parallelism that existed between the upper anvil, upper aluminum surface, lower aluminum surface, and lower anvil. For some of the aluminum cubes, double lining with amalgam on both the upper and lower surfaces was necessary due to additional end irregularities produced during the sample machining and preparation. This method of *in-situ* contact formation between the mechanical compression apparatus and the calibration cubes allowed the consistent application of uniform stress during compression increments. It was thus possible to measure displacements fairly close to the small sample edges with a negligible distortion due to Saint-Venant effects.[33]

The aluminum cubes were compressed by moving the load bar (Fig. 2) upward by small displacement increments. Thus the cubes were compressed in the vertical direction only, between the upper and lower anvils. A series of compression increments were performed, and for each step in the series the force (F) was recorded and used to determine the stress increment $(\Delta F/A)$. Some typical results are presented in Table 1. Prior to and immediately after each compression increment, pre- and postload phase differences $\Delta\varphi_{\text{pre}}$ and $\Delta\varphi_{\text{post}}$ were recorded along all three axes: X, Y, and Z to measure any surface displacements.

4.2 *Tooth Dentin Samples*

Root dentin was obtained from just below the enamel cap of a healthy noncarious human lower first premolar, extracted for valid dental orthodontic reasons. Four samples were cut from the lingual, distal, buccal, and mesial sides of the root, as shown in Fig. 4. The sample sizes were approximately 2×1×1 mm (length along the tooth axis). A water-cooled slow-speed saw (Model 650, South Bay Technologies, San Clemente, California) and a high-speed dental hand piece (TC-95RM, W&H, Austria) mounted on a three-axis minimilling mount and fitted with stainless steel-diamond dental burs (C2 and D1, Strauss and Company, Westport, Connecticut) were used. The size of tooth dentin samples could not be accurately controlled with these instruments, so we could not produce standard sized specimens. However, special care was taken to preserve the dentin sample orientation with respect to its true location in the tooth.

To rule out the possibility of significant crack formation caused by the sawing necessary for sample preparation, a scanning electron microscope (SEM) was used to inspect several cross-sectional surfaces of root dentin. A representative example of a SEM micrograph is shown in Fig. 5. From these inspections it is evident that except for a 3-μm-thick ‘‘smear layer’’ (damaged zone) found on the outer dentin surface, the bulk cross section is undamaged, which suggests that the samples were not affected by the cutting procedures. None of the samples viewed with the SEM revealed any cracking induced by the sawing. During all stages of preparation and subsequent storage, the samples were kept wet or stored in water at 4°C.

The dentin samples were mounted so that load was applied along the *in-vivo* functional tooth direction, namely parallel to the root and sample long axes. They were mounted using a ceramic-filled composite material, designed for dental restorations (Z250, 3M ESPE, Saint Paul, Minnesota) that held the

Table 1 A typical series of load increments, resulting displacements and stresses produced by loading of an aluminum cube.

Compression increment number	Encoded axial position [μm]	Current step displacement increment [$\Delta\mu$m]	Force applied [N]	Force increment [ΔN]	Applied stress per step ($\Delta N/12\ \mathrm{mm}^2$) [MPa]
Preload:	8		19.8		
1	10	1.7	26.3	6.6	0.55
2	12	1.3	32.2	6.0	0.5
3	14	1.5	38.5	6.3	0.53
4	16	1.6	45.4	7.0	0.58
5	17	1.4	51.3	6.1	0.51
6	18	1.5	58.0	6.8	0.57
7	19	1.3	64.0	6.1	0.51
8	21	1.2	70.2	6.5	0.54
9	23	1.9	77.4	7.4	0.62
10	24	1.4	83.0	5.7	0.48
11	25	1.3	89.2	6.2	0.52
12	27	2.0	97.2	8.2	0.68
13	28	1.5	103.6	6.7	0.55
14	30	1.6	110.6	7.2	0.6
15	32	1.7	118.2	7.8	0.65
16	34	1.2	124.2	6.1	0.51
17	35	1.9	132.2	8.1	0.67
18	37	1.7	139.7	7.8	0.65
19	38	1.3	146.4	6.9	0.58
20	40	1.7	154.1	7.8	0.65
21	41	1.2	159.7	5.7	0.48
22	43	1.6	166.8	7.2	0.6
23	45	1.8	174.5	7.8	0.65
24	46	1.5	180.9	6.5	0.54
25	47	1.4	187.4	6.7	0.55
26	49	1.7	195.5	8.3	0.69
27	51	1.7	202.4	7.1	0.59
28	53	1.7	209.6	7.3	0.61
29	55	1.6	217.6	8.2	0.68
30	56	1.4	224.2	6.8	0.57

sample in an upright position and adapted the irregular topography of the sample surface to the base anvil. A less-viscous soft composite material (Z100, 3M ESPE) was then used to cap the sample. The upper anvil was brought into contact with the soft material, which was then polymerized *in situ* using a dental light cure device (LITEX 682, Dentamerica, La Puente, California) for a total of 120 sec from the front and back of the sample. The light curing of both materials ensured that an

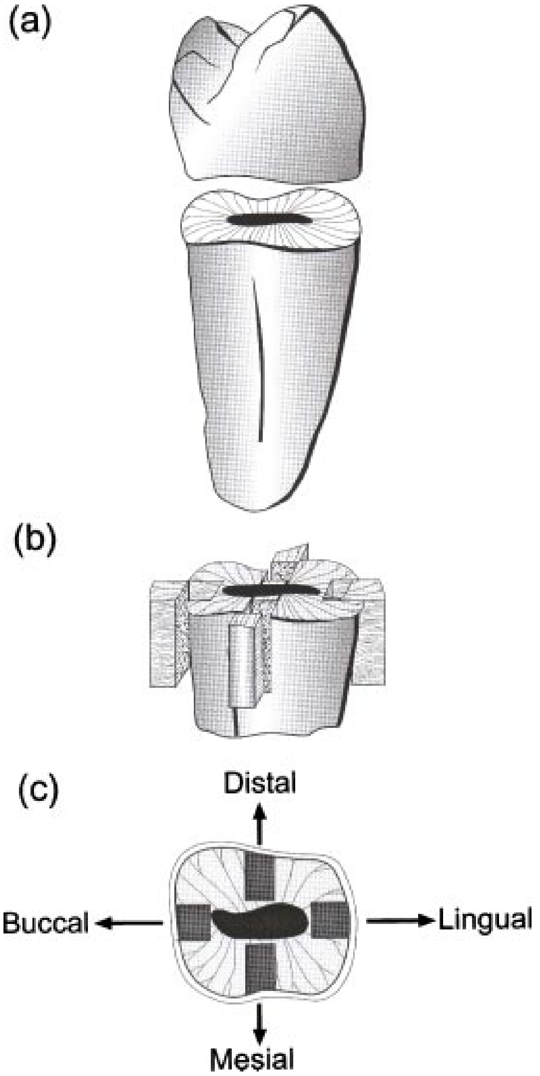

Fig. 4 Schematic illustration of root dentin sample preparation: (a) removal of the tooth enamel covered crown, (b) location of the four samples, and (c) planar view of the sample locations: lingual, distal, mesial and buccal.

intimate and stiff contact with the loading anvils was formed, which required no further dislodging of the samples. After filling the water cell with water and adjusting the optics and light intensities, the speckle interferometry measurements were initiated. A representative mounted dentin sample and a typical speckle image are shown in Fig. 6.

The dentin samples were tested by performing a series of compression stress loads and concomitant strain measurements. It should be noted that the smaller cross-sectional area of our dentin samples, as compared with the calibration aluminum cubes, resulted in larger stress for similar load increments, which produced higher strains.

5 Data Analysis and Experimental Results

We performed a series of experiments to determine the displacements, strains, and Young's modulus for the aluminum calibration cubes and tooth dentin samples. To determine surface displacements with our system, it was necessary to record and analyze the speckle images for each measurement increment, before and after each step of vertical compression in a load series, for each of the three orthogonal directions. For a given experiment, an area of interest (AOI) was chosen so as to avoid inclusion of the sample edges and areas of poor illumination. This allowed the creation of three 2-D modulo 2π matrices of phase differences $\Delta\varphi(i,j)_{\mathrm{pre}}-\Delta\varphi(i,j)_{\mathrm{post}}$, where i and j refer to rows down and columns across the sample. These matrices contained the wrapped phase shift maps, with each element (i,j) corresponding to a small area on the surface of the sample $(\Delta y,\Delta x)$, which we approximate to a point (y,x).

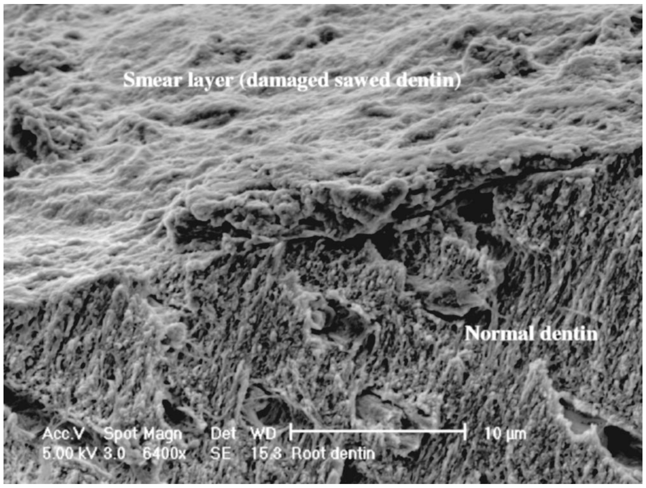

Fig. 5 SEM micrograph of the cross section of cut dentin. A thin smear layer composed of damaged dentin debris is produced on the sawed surface during sample preparation, but does not show any signs of damage propagation into the normal dentin below it, such as cracks.

We now describe the analysis procedure for the vertical axial displacements matrix $v(i,j)$ obtained from the Y-axis interferometer to determine the axial strain. The treatment of the other two directions is essentially the same. Note that in our experiments, the X and Z displacement components were used only to discriminate between measurements of uniformly loaded samples, in which the displacements were primarily axial, and those of samples that underwent significant shear and/or whole body rotation. In this way it was possible to identify and remount poorly loaded samples.

To convert the wrapped phase shift map information into displacement data, it was first necessary to resolve ambiguities caused by the fact that the phase differences are only determined up to an integer multiple of 2π. The ambiguities were resolved only in the AOI using a dedicated software package (ISTRA, Ettemeyer GmbH, Ulm, Germany) that performs the required phase unwrapping. Prior to this unwrapping, some filtering was necessary for the automatic processing to detect the fringes correctly and produce phase difference maps that represent the true surface displacements. Various options for filtering could be used, such as median filtering, filtering in the Fourier domain, or applying convolutions with kernels of various sizes.[34] As we were not concerned with improving image quality, but rather preserving data integrity so as to be able to estimate the gradient of displacement accurately, only minimal averaging was per-

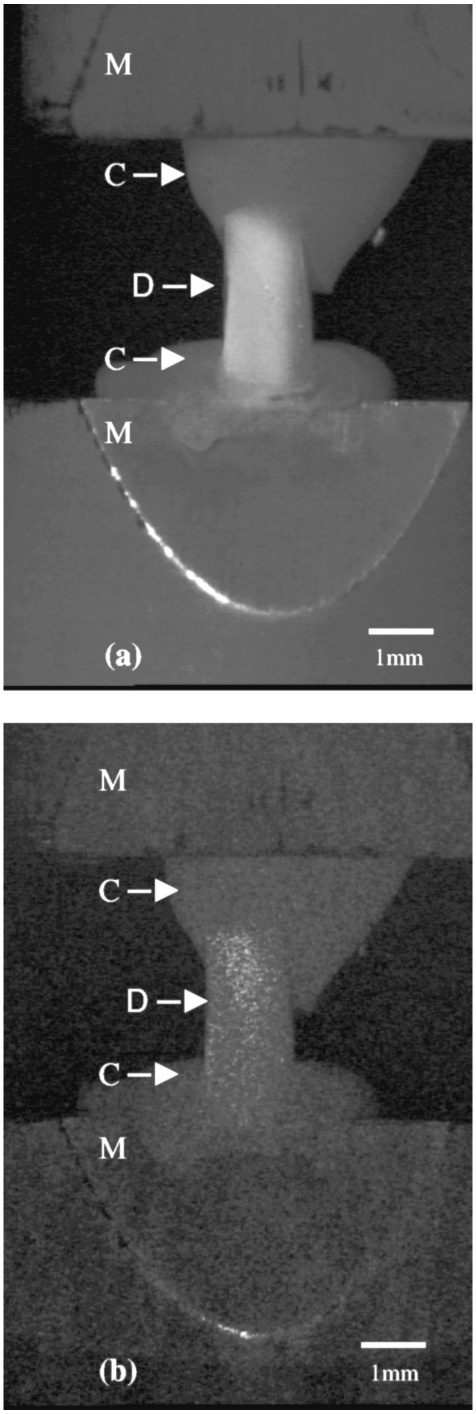

Fig. 6 Mounted dentin sample under compression: (a) dentin sample prior to laser illumination, mounted between metal anvils and held in place with cured composite, and (b) low-contrast speckle image of dentin sample in water with laser illumination. M are the stainless steel metal anvils, C is the composite, and D is the dentin sample.

formed by weighting each point relative to its four nearest neighbors with a ratio of 4 to 1 (a so-called low pass filter). This extent of averaging was found to be the minimum necessary to obtain reproducible estimates of displacements when measuring the aluminum cubes loaded in water.

Once $\Delta\varphi(i,j)_{\text{pre}}-\Delta\varphi(i,j)_{\text{post}}$ at each point was known, it was possible to determine the surface displacements using Eqs. (3) and (4) for each point. Representative wrapped phase maps and corresponding displacement maps are shown in Fig. 7. Figure 7(a) shows the gradual transition from white to black above and on the loaded sample in the center of the image, for the out-of-plane measurement. As is evident, only one fringe is visible, as is typical for all our measurements. Figure 7(b) shows the corresponding pseudo 3-D representation of the displacements map after unwrapping the phases in the AOI in Fig. 7(a), including the scaling factor $\lambda/4\pi$ as given in Eq. (4). Figure 7(c) shows the wrapped phase map for a representative in-plane measurement, and Fig. 7(d) shows the corresponding unwrapped and scaled displacements map of the AOI.

For a quantitative determination of the strain, it was necessary to assume that the vertical displacements map of the AOI could be modeled as a plane with coefficients that represent displacement gradients or slopes along and across the sample. To determine these slopes, and consequently the strains, least-squares regression analysis was used. Regression analysis overcame the effect of the spread of the offset displacement values. Because of the large number (N) of data points obtained for each measurement (typically $N>7000$ points), the standard errors, which are proportional to $1/\sqrt{N}$, were small and the resulting estimates of displacement gradients were precise. We note that it is possible to split the AOI into subareas and determine the different strains in the different subareas of a given AOI on the sample surface.

Since the compression loading was performed in the vertical direction, only the dominant Y component of the displacement needed to be considered for the axial strain calculations. For each stress increment, the slope in the $v(i,j)$ displacement values was estimated from the regression plane in the AOI both along and across the loading axis. This was used to determine the strain based on the strain-displacement equation[32] used for small strains

$$\epsilon_y=\frac{\partial v(y,x)}{\partial y}, \tag{5}$$

in which $v(y,x)$ are the vertical displacements at each point (y,x) on the object surface. Because each point in the displacement map $v(i,j)$ covers an area of approximately $15\times15\ \mu\text{m}$ on the sample surface, we consider $15\ \mu\text{m}$ to be the distance between adjacent rows of measurements on the sample. Estimates of strain were readily obtained by dividing the slope $[\mu\text{m/row}]$ by the width of each row of measurements on the sample. It should be noted that the procedure for finding $v(i,j)$ and ϵ_y can also be used to find the orthogonal displacement field $u(i,j)$ from the X axis interferometer, and the corresponding strain ϵ_x. Thus, the Poisson ratio, which is the ratio of $-\epsilon_x$ to ϵ_y, can be readily found.

Figure 8 shows some representative experimental displacements and strain results for one of the aluminum cubes. Figure 8(a) shows a typical edge view of the vertical displacements map as a function of the line row number along the object for a single compression increment. As is evident, there appear to be marked fluctuations of displacement between neighboring points. These are due to a variety of errors, in-

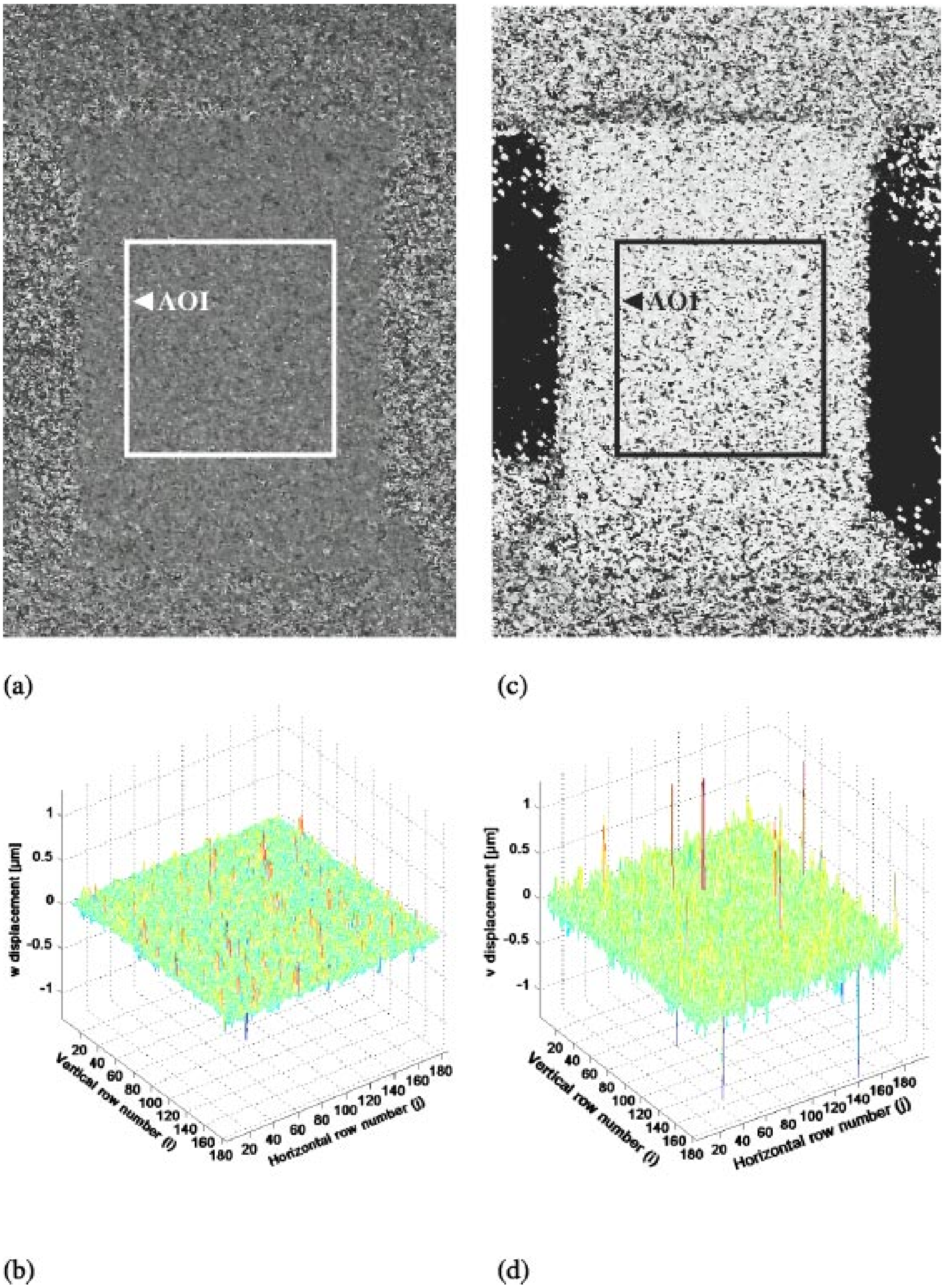

(a) (c)

(b) (d)

Fig. 7 Typical out-of-plane and in-plane wrapped phase-shift maps and corresponding displacement maps. (a) Wrapped out-of-plane phase shift map; AOI denotes the area of interest. (b) Pseudo 3-D representation of the unwrapped and scaled displacement data from the AOI in Fig. 7(a). (c) Wrapped in-plane *Y*-direction phase shift map and selected AOI. (d) Corresponding pseudo 3-D representation of the unwrapped and scaled displacement data from the AOI in Fig. 7(c).

cluding errors in the phase measurements, phase unwrapping algorithm, and laser and detector noises. To compensate for these, the displacement values in the AOI were all used to determine the gradient and obtain the corresponding regression plane. The slope of the edge view, also shown in Fig. 8(a), is 0.12 nm/row. This reflects a gradient in the axial displacement $v(i,j)$ direction along the sample. The slope corresponds to an axial strain of $\epsilon = 0.12/15{,}000 = 8 \cdot 10^{-6}$, since

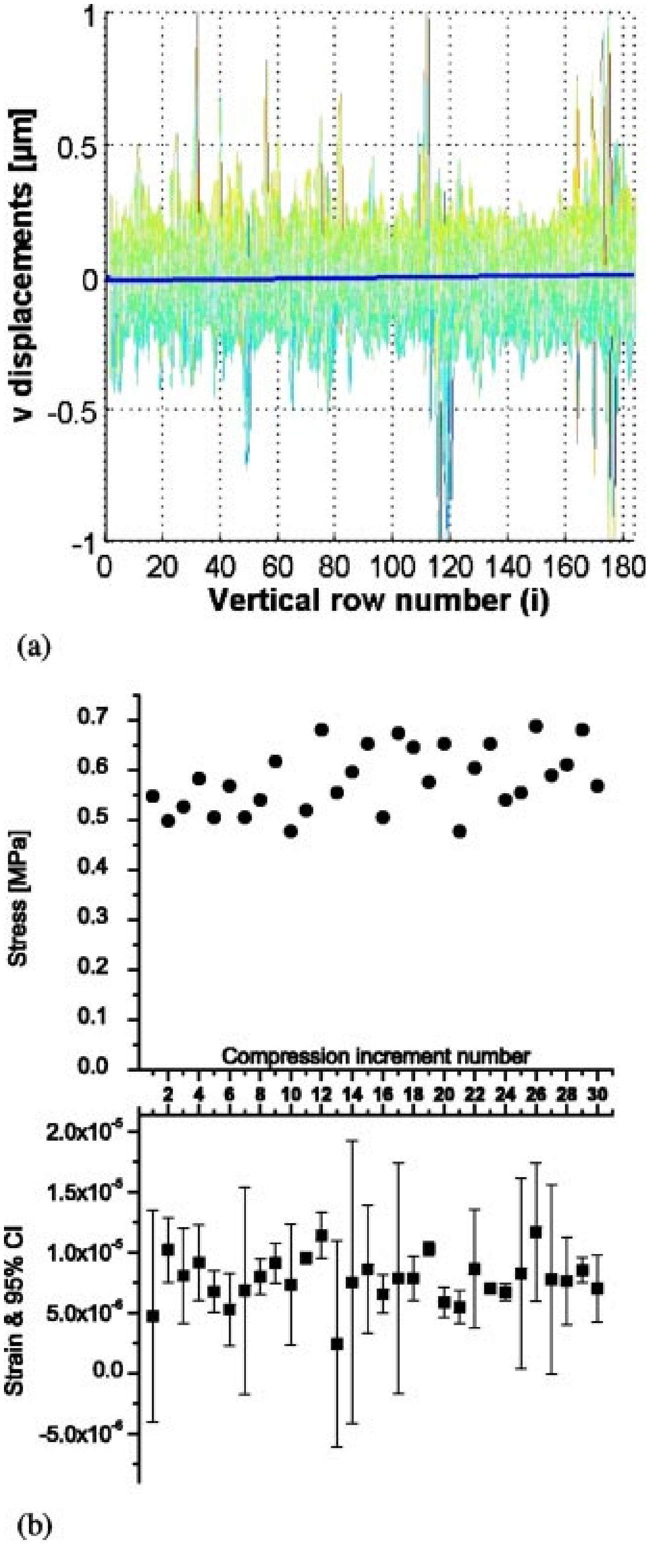

Fig. 8 Experimental displacements, stress, and strain for a representative aluminum cube. (a) Side view of a pseudo 3-D projection of displacements for a single compression cycle, with a corresponding edge view of the regression plane with a slope of 0.00012 [μm/row]. (b) plot of strain and stress as functions of compression cycles, with the corresponding 95% confidence intervals shown by the vertical bars.

Table 2 Estimates of Young's modulus (*E*) for aluminum samples measured under compression in water. The normality *P* value is based on the Shapiro-Wilk normality test.

	Slope of the stress-strain curves [GPa]		Estimated best *E* [GPa]		
Sample number	*E*	95% CI	*E*	Normality *P* value	Number of compression increments
1	75.8	74.9 to 76.7	74.8	0.693	30
2	68.8	67.1 to 70.6	68.6	0.266	25
3	73.4	70.5 to 76.3	72.9	0.203	12
Average	72.7		72.1		

the distance between each row of measurements on the sample was 15 $\mu\text{m}=15{,}000$ nm.

Similar measurements were obtained for 30 sequential compression increments as shown in Table 1, where the cumulative loads increased by approximately equal increments. The stresses produced in these compression increments are shown in Fig. 8(b), as well as the results of strain and confidence intervals (CI) calculated for each increment. As noted before, in all our measurements we checked that whole body rotation and shear were negligible.

Using the results shown in Fig. 8, we now use two different though related methods to determine the Young's modulus (E) of the sample. In one, we plot the cumulative stress against the cumulative strain, while in the other we determine the best compliance estimate to find the estimated best E. By the first method, an example of which is shown in Fig. 9(a), we determined the stress-strain E from the slope of the curve. Using a simple linear regression fit, the E for this cube was calculated to be 75.8 GPa. This, together with the results for two other aluminum cubes, are shown in Table 2. It can be argued that the use of a regression model for such a fit is not valid, because the values of the cumulative strains are not independent of each other. Therefore, we propose another method of determining E, based on the individual increments of strain that are truly independent of each other.

A histogram of individual compliance estimates is obtained by dividing the individual strain values by the stress of each compression increment [Fig. 8(b)]. An example of a histogram for one cube is shown in Fig. 9(b). The individual compliance estimates have a distribution for which a measure of central tendency can be established, such as the arithmetic mean. We chose the best compliance estimate (c) to be the mean of this distribution, which for the cube shown in Fig. 9(b) has a value of $c=1.3367\cdot 10^{-5}\,[\text{MPa}^{-1}]$. Provided that the distribution of the compliance estimates around this mean is reasonably normal, the estimate of the best E is found from the inverse of the best compliance estimate. The normality of the results shown in Fig. 9(b) was confirmed to the 0.05% level, using the Shapiro-Wilk normality test ($P>0.6$). Accordingly, the estimated best E is $1/c=74.8\,\text{GPa}$ for this aluminum cube. The values for the other two cubes and their corresponding probabilities of normality are shown in Table 2.

The results summarized in Table 2 show Young's modulus, obtained by both stress-strain *E* and estimated best *E* for each cube, and the ranges of 95% confidence intervals (CI) for each measurement of the stress-strain *E* to provide an estimate of the error. Table 2 also shows the probability of normality and the number of compression increments applied to each cube. The average estimated *E* values for both analytical methods are very close to 72 GPa. The published value for Young's modulus in tension, reported for this type of aluminum, is 69 GPa, and the compression Young's modulus is estimated to be 2% higher, i.e., 70.4 GPa.[35] Thus our average ESPI measured values are within 3% of the nominal value for aluminum measured by other techniques.

Finally, we performed a series of experiments to determine the strain and Young's modulus of dentin in water. The surface strain was determined, and the stress-strain *E* and estimated best *E* were using the same method described for aluminum. Table 3 summarizes the results of these experiments. Note that the opposing samples (lingual-buccal and mesial-distal) produced similar results, but the average of these modulus values for each pair are very different, namely 15.0/14.6 GPa and 21.3/19.4 GPa, using estimated best *E*/stress-strain *E*, respectively.

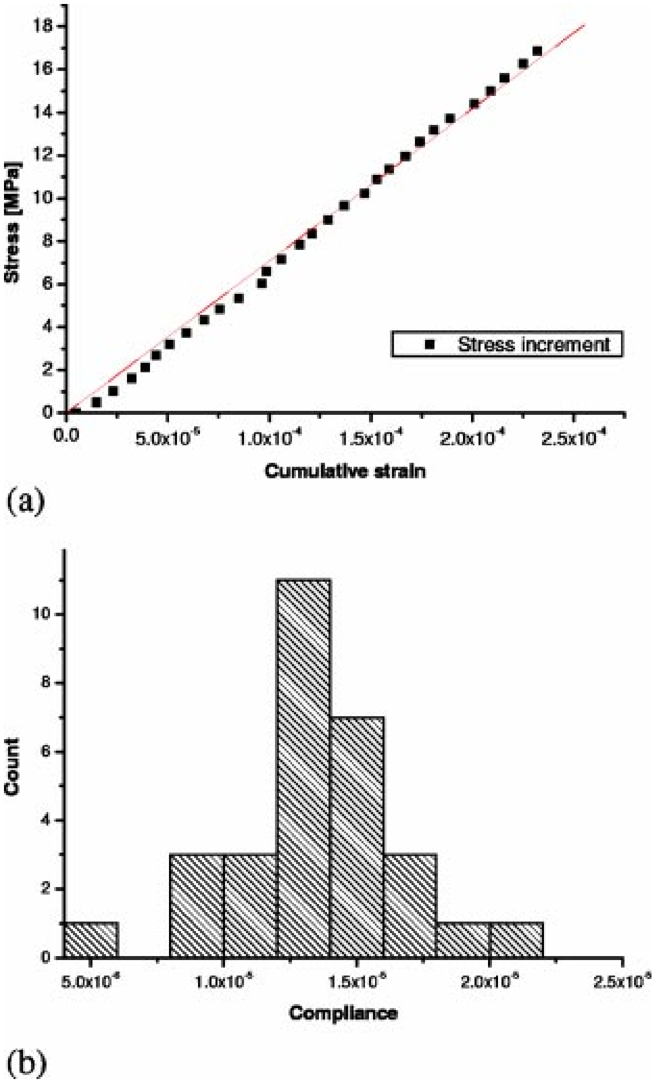

Fig. 9 Determination of Young's modulus for a representative aluminum cube. (a) Typical stress-strain curve whose slope is the Young's modulus $E=75.8$ GPa; (b) histogram of the individual compliance estimates, produced from the ratio between the strain and stress measurements in Fig. 8(b). The best compliance estimate is the mean of the histogram and has a value of $c=1.3367\cdot 10^{-5}$, with a corresponding modulus of $E=74.8$ Gpa.

6 Discussion

The results show that our method can provide quantitative noncontact and direct measurements of displacements and strains for aluminum measured in water, which can be used to obtain precise estimates of the elastic properties. This approach has been applied to human tooth root dentin. While compression measurements are generally complicated to perform and interpret, they are essential to characterize and understand the structural design of hard biological tissues, which often perform load-bearing tasks. In teeth and particularly root dentin, compression is probably the most significant type of load encountered, although other forms of stress are known to occur.[36,37]

We combined the well-established phase shifting interferometery method[18,19] with a mechanical loading device capable of mounting and loading samples in water. The loading configuration can be readily adapted to handle a range of sample sizes and shapes. This includes, for example, whole teeth (at least of humans), small bones, and shells, ranging from several centimeters in length down to very small 3-D samples of

Table 3 Estimates of Young's modulus (*E*) for dentin samples measured under compression in water. The normality *P* value is based on the Shapiro-Wilk normality test.

		Slope of the stress-strain curves [GPa]		Estimated best *E* [GPa]		
Sample number	Location in the root	*E*	95% CI	*E*	Normality *P* value	Number of compression increments
1	Lingual	13.8	13.2 to 14.4	14.2	0.195	12
2	Distal	20.6	18.7 to 22.4	21.8	0.392	11
3	Buccal	15.3	14.7 to 15.8	15.7	0.975	11
4	Mesial	18.2	17.8 to 18.7	20.8	0.127	9

a millimeter or so in each dimension. The use of a light-cure dental material that is homogenous and isotropic and can be polymerized and cross-linked when it is in contact with all surfaces under stress has proven to be reliable for applying axial loads and minimizing off-axis trajectories of force, which lead to extensive rotation, bending, and shear. It allows for specimens of irregular shape to be mounted, and it is easily removed so that the same specimen can be remounted in a different orientation; a major advantage in biomechanical studies.

The fact that the speckle interferometry method is truly noncontact alleviates the need to glue anything directly to a smooth surface, as is the case for Moiré interferometry,[16] and most importantly allows for repeated measurements to be made in different orientations on the same specimen. Thus key questions relating to the anisotropy and homogeneity of biological materials can be addressed. Finally, almost all biological specimens need to be examined in a hydrated environment, both because this is the nature of the *in-vivo* conditions in which they normally function, and to avoid drying artifacts such as microcracking. This instrument should therefore have many applications for the study of biological tissues.

We used the experiments on the aluminum samples to calibrate the system and to optimize many of the parameters needed to measure samples in water. This included assessing the limitations of sample size, selection of lenses and apertures, and determination of suitable magnification, illumination settings, water cell design, and experimental procedures. The results obtained for measurements of aluminum 6061 yield moduli that are within 3% of the reported values for this material, namely just over 70 GPa for compression. The data shown in Table 2 show the Young's moduli of the aluminum cubes calculated in two different ways. Although all give reasonable values, in our opinion, the estimated best E values are more reliable than the stress-strain E, because the latter involves an accumulation of errors due to the need to sum the strain values that have large CIs.

Of much concern is the magnitude of shear during compression testing. If significant shear develops, the amount of axial loading will be overestimated and needs to be accounted for. For relatively stiff materials, this is probably more problematic than for most biological samples, because the higher the stiffness, the higher the susceptibility to off-axis trajectories of force due to the inevitable flexibility of the mechanical compression apparatus. However, in our experiments, even with the aluminum samples that have a modulus which is about 35% of the stainless steel anvils, shear strain was found to be at least 1 order of magnitude smaller than the axial strain. The shear strain was estimated from the gradients of the $u(i,j)$ and $v(i,j)$ displacements for the Y and X directions, respectively. We point out that by using a relatively thin homogenous lining of a polymerizable material, it was possible to establish a good contact between the sample upper and lower surfaces and the compressing anvils, which resulted in the smallest shear strains and the most reproducible results.

In general, dentin samples with inherent high water content are complicated to measure with optical methods due to their translucency and poor surface reflectivity. For these samples, the signal-to-noise ratio in the images is relatively low because of a reduced contrast of the speckle fields. The water affects the phase directly because of microflowing and convection currents that occur during and after each compression increment. Water also affects the refractive index of the dentin, which creates additional reflections from within the sample during compression steps. Yet in our approach with the large number of sampled points for every compression increment and the repeated measurements by small displacements of the sample, it was possible to precisely determine the strain and Young's modulus in compression.

The moduli obtained for the dentin samples from four locations within a single tooth are within the range of reported values[12] and were obtained after performing calibration measurements using the aluminum cubes. We noted that the Young's moduli of opposing mesiodistal samples are about 40% stiffer than the opposing buccul-lingual samples. This, to our knowledge, has not been previously reported, and may indicate an interesting structural design embedded in the root of the tooth. The biological and clinical significance of these observations remains to be determined.

The quality of the data is such that the measurements can be recalculated for subareas of the AOI. We have done this and can show that displacements and strain can be determined if the subareas in the AOI are limited to approximately 200 μm wide and 400 μm along the axial direction. Thus strains can be compared over submillimeter distances—the mesoscale. This opens up the exciting possibility of mapping displacements of whole teeth as well as teeth sections to better understand the contribution of the graded structure of dentin to the overall tooth deformation during function. This same approach is directly applicable to measurements of other members of the bone family of materials.

7 Conclusions

Phase shifting interferometry offers the opportunity to make direct measurements of the deformation patterns and elastic constants of wet biological materials at mesoscale dimensions. Having solved many of the technical problems associated with the measurements and the data analysis, questions can now be addressed concerning the relations between structural variations and mechanical properties of biological materials. Studies designed to answer these questions are not limited to measuring only the elastic properties on planar surfaces, but can be extended to include 3-D deformation analysis of irregular-shaped bodies, both in the elastic and in the visco-elastic regime, and possibly microfracture formation. Of particular interest will be studies involving comparison between natural biological materials and synthetic replacement parts, such as dental restorations, where the manner in which these different materials work together needs to be understood. Other studies could include dynamic monitoring of crack development, investigations of fatigue, and a better understanding of the influence of graded structures on mechanical properties. Finally, it may be possible to use phase shifting interferometry to investigate differences in properties that may exist in the bones and teeth of individuals differing in age, sex, and states of disease.

Acknowledgments

We thank Benjamin Sharon, David Leibovitz, Yossi Shopen, Gershon Elazar, and Yossi Leibovitz for their superb technical assistance, and Giancarlo Pedrini and Ron Shahar for many helpful discussions. Author Weiner is the incumbent of the Dr. Walter and Dr. Trude Burchardt Professorial Chair of Structural Biology. Author Friesem is the incumbent of the Peter and Carola Kleeman Professorial Chair of Optical Sciences. Support for this research was provided from grant 2 RO1 DE 006954 from the National Institute of Dental and Craniofacial Research, The Weizmann Institute of Science, and an Isaiah Travel Bursary from the Academic Study Group for Israel and the Middle East.

References

1. S. A. Wainwright, W. D. Biggs, J. D. Currey, and J. M. Gosline, *Mechanical Design in Organisms*, Princeton University Press, Princeton (1976).
2. J. D. Currey, *Bones: Structure and Mechanics*, Princeton University Press, Princeton (2002).
3. W. Tesch, N. Eidelman, P. Roschger, F. Goldenberg, K. Klaushofer, and P. Fratzl, ‘‘Graded microstructure and mechanical properties of human crown dentin,’’ *Calcif. Tissue Int.* **69**, 147–157 (2001).
4. R. A. Robinson and S. R. Elliot, ‘‘The water content of bone,’’ *J. Bone Jt. Surg., Am. Vol.* **39-A**(1), 167–188 (1957).
5. M. Braden, ‘‘Biophysics of the tooth,’’ in *Physiology of Oral Tissues*, Y. Kawamura, ed., pp. 1–37, S. Karger, Basel, New York (1976).
6. N. Meredith, M. Sheriff, D. Setchell, and S. Sivanson, ‘‘Measurements of the microhardness and Young’s modulus of human enamel and dentin using an indentation technique,’’ *Arch. Oral Biol.* **41**(6), 539–545 (1996).
7. H. H. H. Xu, D. T. Smith, S. Jahanmir, E. Romberg, J. R. Kelly, V. P. Thompson, and E. D. Rekow, ‘‘Indentation damage and mechanical properties of human enamel and dentin,’’ *J. Dent. Res.* **77**(3), 472–480 (1998).
8. J. D. Currey, ‘‘Tensile yield in compact bone is determined by strain, post-yield behaviour by mineral content,’’ *J. Biomech.* **37**, 549–556 (2004).
9. J. Kinney, M. Balooch, S. Marshall, G. Marshall, and T. Weihs, ‘‘Young’s modulus of human peritubular and interturbular dentine,’’ *Arch. Oral Biol.* **41**(1), 9–13 (1996).
10. H. Fong, M. Sarikaya, S. N. White, and M. L. Snead, ‘‘Nanomechanical properties profiles across dentin-enamel junction of human incisor teeth,’’ *Mater. Sci. Eng., C* **7**, 119–128 (2000).
11. G. W. Marshall, M. Balooch, R. R. Gallagher, S. A. Gansky, and S. J. Marshall, ‘‘Mechanical properties of the dentinoenamel junction: AFM studies of nanohardness, elastic modulus and fracture,’’ *J. Biomed. Mater. Res.* **54**, 87–95 (2001).
12. J. Kinney, M. Balooch, G. W. Marshall, and S. J. Marshall, ‘‘A micromechanics model of the elastic properties of human dentin,’’ *Arch. Oral Biol.* **44**, 813–822 (1999).
13. A. Kishen, U. Ramamurty, and A. Asundi, ‘‘Experimental studies on the nature of property gradients in the human dentine,’’ *J. Biomed. Mater. Res.* **51**, 650–659 (2000).
14. J. L. Katz, P. Spencer, T. Nomura, A. Wagh, and Y. Wang, ‘‘Micromechanical properties of demineralized dentin collagen with and without adhesive infiltration,’’ *J. Biomed. Mater. Res.* **66A**, 120–128 (2003).
15. J. L. Katz, S. Bumrerraj, J. Dreyfuss, Y. Wang, and P. Spencer, ‘‘Micromechanics of the dentin/adhesive interface,’’ *J. Biomed. Mater. Res.* **58**, 366–371 (2001).
16. J. D. Wood, R. Z. Wang, S. Weiner, and D. H. Pashley, ‘‘Mapping of tooth deformation caused by moisture change using Moiré interferometry,’’ *Dent. Mater.* **19**, 159–166 (2003).
17. R. Wang and S. Weiner, ‘‘Strain-structure relations in human teeth using Moiré fringes,’’ *J. Biomech.* **31**(2), 135–141 (1998).
18. P. K. Rastogi, ‘‘Measurement of static surface displacements, derivatives of displacements and three-dimensional surface shapes—examples of applications to non-destructive testing,’’ in *Digital Speckle Pattern Interferometry and Related Techniques*, P. K. Rastogi, Ed., pp. 141–224, John Wiley and Sons, Chichester, UK (2001).
19. R. Jones and C. Wykes, *Holographic and Speckle Interferometry*, 2nd ed., Cambridge University Press, Cambridge (1989).
20. J. Horta, W. Brostow, G. Martinez, and V. M. Castano, ‘‘Characterization of bones by speckle interferometry,’’ *J. Med. Eng. Technol.* **27**(2), 49–53 (2003).
21. D. Zhang, D. D. Arola, and J. A. Rouland, ‘‘Evaluating the elastic modulus of bone using electronic speckle pattern interferometry,’’ *Exp. Tech.* **25**(5), 32–34 (2001).
22. A. Kishen and A. Asundi, ‘‘Investigations of thermal property gradients in the human dentine,’’ *J. Biomed. Mater. Res.* **55**, 121–130 (2001).
23. A. Oulamara, G. Tribillon, and J. Duvernoy, ‘‘Biological activity measurement on botanical specimen surfaces using a temporal decorrelation effect of laser speckle,’’ *J. Mod. Opt.* **36**(2), 165–179 (1989).
24. S. J. Kirkpatrick and B. W. Brooks, ‘‘Micromechanical behavior of cortical bone as inferred from laser speckle data,’’ *J. Biomed. Mater. Res.* **39**, 373–379 (1998).
25. S. J. Kirkpatrick and M. J. Cipolla, ‘‘High resolution imaged laser speckle strain gauge for vascular applications,’’ *J. Biomed. Opt.* **5**(1), 62–71 (2000).
26. D. D. Duncan and S. J. Kirkpatrick, ‘‘Processing algorithms for tracking speckle shifts in optical elastography of biological tissues,’’ *J. Biomed. Opt.* **6**(4), 418–426 (2001).
27. G. Pedrini, H. J. Tiziani, and Y. Zou, ‘‘Digital double pulse TV holography,’’ *Opt. Lasers Eng.* **26**, 199–219 (1997).
28. K. A. Stetson and W. R. Brohinsky, ‘‘Electrooptic holography and its application to hologram interferometry,’’ *Appl. Opt.* **24**(21), 3631–3637 (1985).
29. R. Ritter, K. Galanulis, D. Winter, E. Muller, and B. Breuckmann, ‘‘Notes on the application of electronic speckle pattern interferometry,’’ *Opt. Lasers Eng.* **26**, 283–299 (1997).
30. G. T. Reid, ‘‘Automatic fringe pattern analysis: A review,’’ *Opt. Lasers Eng.* **7**, 37–68 (1986).
31. J. M. Huntley, ‘‘Automated fringe pattern analysis in experimental mechanics: a review,’’ *J. Strain Anal. Eng.* **33**(2), 105–125 (1998).
32. A. Asundi, ‘‘Introduction to engineering mechanics,’’ in *Topics in Applied Physics: Photomechanics*, P. K. Rastogi, Ed., pp. 33–54, Springer-Verlag, Heidelberg (2000).
33. R. C. Hibbeler, *Mechanics of Materials*, 3rd ed., Prentice Hall, Englewood Cliffs, NJ (1997).
34. J. M. Huntley, ‘‘Automated analysis of speckle interferograms,’’ in *Digital Speckle Pattern Interferometry and Related Techniques*, P. K. Rastogi, Ed., pp. 59–140, John Wiley and Sons, Chichester, UK (2001).
35. H. E. Boyer and T. L. Gall, *Metals Handbook*, ASM Intl., Materials Park, OH (1985).
36. A. Asundi and A. Kishen, ‘‘Advanced digital photoelastic investigations on the tooth-bone interface,’’ *J. Biomed. Opt.* **6**(2), 224–230 (2001).
37. A. Kishen and A. Asundi, ‘‘Photomechanical investigations on post endodontically rehabilitated teeth,’’ *J. Biomed. Opt.* **7**(2), 262–270 (2002).